

PAPER • OPEN ACCESS

## Polarization-resolved supercontinuum generated in a germania-doped photonic crystal fiber

To cite this article: Nicolas Couture *et al* 2021 *J. Phys. Photonics* **3** 025002

View the [article online](#) for updates and enhancements.



## PAPER

## OPEN ACCESS

RECEIVED  
28 August 2020REVISED  
2 February 2021ACCEPTED FOR PUBLICATION  
18 February 2021PUBLISHED  
9 March 2021

Original content from this work may be used under the terms of the [Creative Commons Attribution 4.0 licence](https://creativecommons.org/licenses/by/4.0/).

Any further distribution of this work must maintain attribution to the author(s) and the title of the work, journal citation and DOI.



# Polarization-resolved supercontinuum generated in a germania-doped photonic crystal fiber

Nicolas Couture<sup>1</sup> , Rachel Ostic<sup>1</sup> , P Harshavardhan Reddy<sup>2,3</sup> , Ajoy Kumar Kar<sup>4</sup>, Mukul Chandra Paul<sup>3</sup> and Jean-Michel Ménard<sup>1</sup>

<sup>1</sup> Department of Physics, University of Ottawa, Ottawa, ON K1N 6N5, Canada

<sup>2</sup> Academy of Scientific and Innovative Research, CSIR-CGCRI Campus, Kolkata 700032, India

<sup>3</sup> Fiber Optics and Photonics Division, CSIR-CGCRI Campus, Kolkata 700032, India

<sup>4</sup> Institute of Photonics and Quantum Sciences, Heriot-Watt University, Riccarton Campus, EH14 4AS Edinburgh, United Kingdom

E-mail: [jean-michel.menard@uottawa.ca](mailto:jean-michel.menard@uottawa.ca)

**Keywords:** supercontinuum generation, photonic crystal fibers, spectrometers, depolarization, nonlinear optics, fiber optics

Supplementary material for this article is available [online](#)

## Abstract

We characterize the polarization properties of a supercontinuum (SC) generated in a GeO<sub>2</sub>-doped photonic crystal fiber (PCF) to reveal the interplay between nonlinear broadening mechanisms of a pulse propagating in two independent fundamental modes associated to the principal axes of the fiber. Notably, we resolve self-phase modulation, self-shifted Raman solitons and dispersive waves within a set of orthogonal polarization states as they contribute to generate a broad spectrum spanning from 450 to 2150 nm. Interestingly, our experimental results feature a high degree of polarization at the edges of the spectrum in comparison to the region near the pump wavelength. We show that this modulation is caused by nonlinear spectral broadening. We also identify an additional depolarization mechanism preferentially acting on shorter wavelengths, indicative of a Rayleigh-like scattering effect due to the presence of intrinsic sub-wavelength defects in the fiber. Experiments rely on a free-space grating-based monochromator and a broadband polarizer to monitor the output SC and its linear polarization components along the principal axes of the PCF. Our results and experimental technique pave the way toward an improved standard for the characterization of broadband optical spectra and more efficient implementation of highly nonlinear fibers in a large range of polarization-sensitive applications.

## 1. Introduction

The ability to rely on nonlinear optical phenomena to convert a narrow laser spectral linewidth into a broad frequency spectrum, also called supercontinuum (SC), has enabled many applications in optical coherence tomography (OCT), photonic device testing, and optical communications [1–3]. The high spatial coherence of broadband, fiber-based sources is also ideal for applications in optical microscopy [4, 5]. Although silica-based solid-core optical fibers are most commonly used to produce intense and broad SC, there has been a recent interest to develop broadband sources in different optical media to avoid some limitations imposed by silica. Specialty fibers like hollow-core photonic crystal fibers (PCFs) [6–9] and fibers made of soft glasses, like fluoride [10–13] or chalcogenide [14–17], have notably been used to generate SC extending to the ultraviolet (UV) or mid-infrared (MIR) regions, where silica is strongly absorptive [13]. Moreover, pure germania (GeO<sub>2</sub>) fibers and GeO<sub>2</sub>-doped silica fibers have attracted interest both because of their transparency in the MIR region and the fact that their fabrication relies on well-established drawing methods for silica fibers [18, 19]. For instance, an SC spectrum extending beyond 3  $\mu\text{m}$  was achieved in a highly germania-doped fiber with a record optical power of 1.44 W [19].

In general, small imperfections and inhomogeneities in all types of fibers are inevitable due to intrinsic glass impurities and the high sensitivity of the drawing process to environmental changes and vibrations. These defects can lead to polarization changes during optical propagation [20], which are detrimental to

many applications such as OCT [21]. To minimize these changes, techniques relying on stress rods and high core ellipticity are used to obtain polarization-maintaining fibers, which induce a large birefringence between principal fiber axes that minimizes polarization crosstalk. As a result, the fiber birefringence can be a simple and useful metric to describe the ability of a fiber to maintain a linear polarization state. However, this value is typically defined at a single wavelength and it does not describe the complex polarization landscape of a broad spectrum generated by nonlinear effects in the fiber [22]. This exhaustive information is hard to access due to the lack of proper experimental equipment to study broadband polarization properties. For example, optical spectrum analyzers (OSAs) typically used to measure spectral power are not able to analyze the polarization states of an SC associated to the principal axes of the fiber. More complex configurations were used to investigate polarization properties, but they were limited to spectra extending over an octave or less [23].

In this work, we use a free-space, broadband, and polarization-resolving spectrometer to fully characterize the spectral and linear polarization properties of an SC generated inside a germania-doped silica PCF. More specifically, we investigate depolarization within a spectral region extending from 450 to 2150 nm as we vary the input polarization and pulse energy. A number of theoretical studies of SC generated in fibers have been performed in an attempt to explore the effect of varying input pulse parameters, birefringence, and fiber length on the state of polarization of the output spectrum [23–25]. These works are complemented by many experimental studies which have focused on studying SC by changing the input polarization and power [23, 24, 26–28], but, until now, there has been no demonstrated technique allowing experimentalists to fully investigate the polarization properties of an ultrabroadband spectrum. In this work, we unveil wavelength-dependent depolarization effects attributed to optical propagation and nonlinear interactions and extract the degree of polarization (DOP) of each spectral component of an SC. To our knowledge, this is the first comprehensive experimental study of the interplay between polarization states in a fiber-based broadband source spanning more than two octaves. We notably report a high DOP toward the edges of the spectrum and a negligible polarization crosstalk during the nonlinear spectral broadening process, even in a low-birefringence fiber. Interestingly, we observe a consistently lower DOP at shorter wavelengths, which can be attributed to a depolarization mechanism associated to Rayleigh-like scattering in the fiber. The novel experimental configuration introduced in this work records polarization components of the spectrum associated to each principal axis of the PCF and reveals wavelength-dependent depolarization processes and features unaccounted for in previous theoretical and experimental studies. We believe such a configuration will help establish new standards for SC characterization and evaluating the polarization maintaining capabilities of optical fibers.

## 2. Methods

For these experiments, we fabricate a silica-based highly nonlinear PCF with 50 mol% GeO<sub>2</sub>-doped core (figure 1). We use a two-step stack and draw method [29] with a central GeO<sub>2</sub>-doped core obtained with the procedure described in [30]. Briefly, capillaries are stacked around the solid doped rod, inserted into a jacket and drawn to a 2 mm diameter cane with adjustable pressure controlling the spacing between the end-sealed capillaries to ensure the proper air-clad configuration. The cane is then inserted into an 8 mm outer diameter jacket and the overall size is reduced to a fiber diameter of 125 μm. The final PCF has a loss of ~0.5 dB m<sup>-1</sup> and a low birefringence  $< 1 \times 10^{-6}$  at a wavelength of 1030 nm, measured with the cutback technique. A scanning electron micrograph (SEM) image of the PCF is shown in figures 1(a) and (b). The core has an average diameter of 4.7 μm with an ellipticity  $\varepsilon = 0.17$ , and the air-cladding bridges branching off from the core have a 0.8 μm width. Figure 1(c) shows a relatively high and homogenous doping level of GeO<sub>2</sub> across the core area of the fiber as measured with electron probe microanalysis. The resulting step index  $n_{\text{core}} - n_{\text{cladding}} \sim 0.045$  further increases the spatial confinement of light in the core, reducing the modal effective area and enhancing nonlinear effects.

A Yb:KGW ultrafast source is used for SC generation. The laser delivers 185 fs pulses centered at a wavelength of 1030 nm, near the zero-dispersion wavelength of the PCF at 1047 nm. The pulse energy launched into the 0.8 m long PCF is adjusted with a half-wave plate (HWP) and a polarizer, with the HWP angle finely controlled by a motorized rotation mount. A second motorized HWP is located immediately before the fiber to control the input polarization. The coupling efficiency is 40% and it allows us to inject up to 36 nJ pulse energy into the PCF without damaging the input facet. The output SC is collimated with an off-axis parabolic mirror to avoid chromatic aberrations. An ultrabroadband wire grid polarizer with an extinction ratio  $> 10^4$  between 500 and 2600 nm located in front of the free-space spectrometer selects the linear polarization to be analyzed. Orthogonal polarization components along the vertical (*V*) and horizontal (*H*) directions, respectively, corresponding to the transverse electric (TE) and transverse

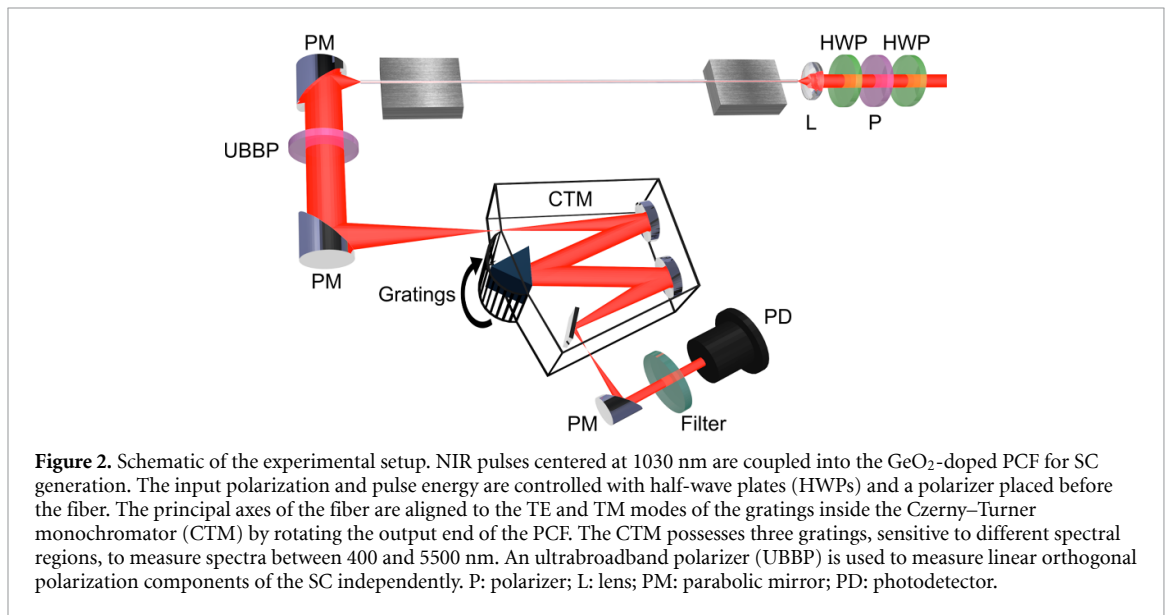
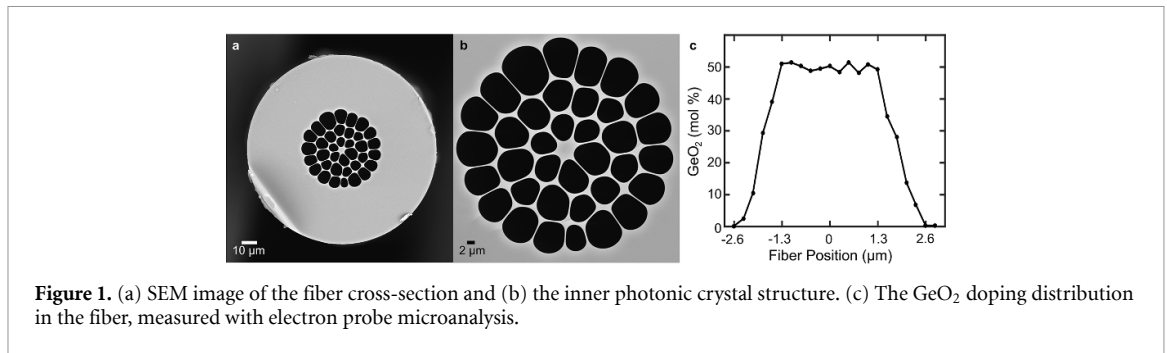


**Table 1.** Gratings, spectral filters, and photodiodes used to collect data in four spectral windows and to calibrate the spectrometer.

Wavelength range (nm)	Gratings		Spectral filter (long-pass)	Photodetector
	Lines mm <sup>-1</sup>	Blaze wavelength (nm)		
400–775	1200	750	None	Si
775–1100	1200	750	750 nm	Si
1100–1800	600	1500	1100 nm	InGaAs
1800–2300	300	3000	1500 nm	InAs

magnetic (TM) modes of the grating inside the spectrometer, are measured successively as we vary the input pulse conditions. The orientation of the end facet of the fiber is adjusted with a rotation mount to ensure that the fiber's principal axes also align with the *V* and *H* orientations. To minimize stress-induced depolarization effects, we keep a 30 cm minimum bend radius and use glue to secure the fiber ends in their respective *v*-grooves. It has been shown, in previous studies and in our tests, that standard fiber clamping mechanisms using magnets enhance polarization crosstalk due to directional pressure [31]. In this paper, we use the term 'crosstalk' to describe any energy transfer between orthogonally polarized optical components aligned along the principal axes of a fiber.

We resolve the spectral power with a customizable Czerny–Turner configuration monochromator employing three different gratings—allowing for spectroscopic measurements from 400 to 5500 nm. Our system, shown in figure 2, also utilizes three interchangeable photodetectors, sensitive to different regions of the spectrum, and, in some cases, spectral filters that prevent the detection of higher diffraction orders from the grating (see table 1). An off-axis parabolic mirror focuses the SC into the spectrometer and motorized slits ensure a constant spectral resolution of 0.7 nm for all recorded data in our experiments. A lock-in amplifier synchronized to the laser's repetition rate is used to minimize the ambient noise while recording spectra. Finally, the spectrometer is calibrated by applying the response functions of all optical components and gratings in our setup for both *V* and *H* polarization components to the measured SC.

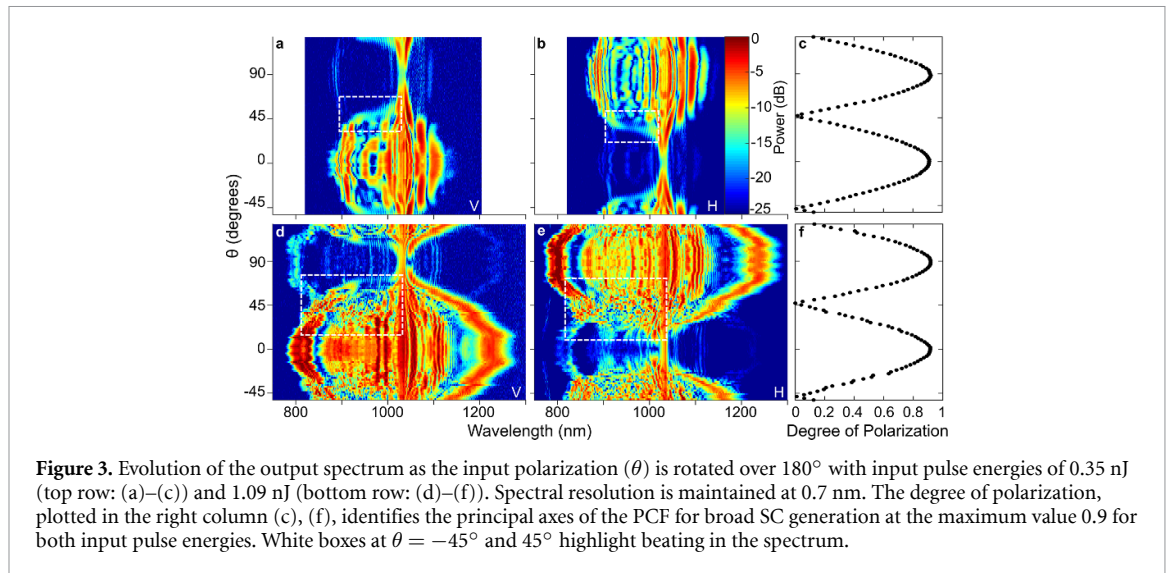


**Figure 3.** Evolution of the output spectrum as the input polarization ( $\theta$ ) is rotated over  $180^\circ$  with input pulse energies of 0.35 nJ (top row: (a)–(c)) and 1.09 nJ (bottom row: (d)–(f)). Spectral resolution is maintained at 0.7 nm. The degree of polarization, plotted in the right column (c), (f), identifies the principal axes of the PCF for broad SC generation at the maximum value 0.9 for both input pulse energies. White boxes at  $\theta = -45^\circ$  and  $45^\circ$  highlight beating in the spectrum.

### 3. Results and discussion

We first monitor the SC at relatively low input pulse energies (0.35 nJ and 1.09 nJ) while rotating the linear input polarization angle ( $\theta$ ) by  $180^\circ$  (figure 3). The principal axes of the PCF at  $\theta = 0^\circ$  and  $90^\circ$  correspond to the maximum spectral broadening. At the lowest input pulse energy (figures 3(a) and (b)), the spectrum splits into multiple closely spaced lobes from the pump ( $\lambda = 1030$  nm), indicative of self-phase modulation (SPM). These lobes are still present in the data set taken at higher pulse energy but they are more numerous and they merge to fill in the entire area surrounding the pump at  $\theta = 0^\circ$  in figure 3(d) and at  $\theta = 90^\circ$  in figure 3(e). This continuous inner section of the spectrum around the pump at 1.09 nJ is framed by a Raman soliton-dispersive wave pair. The similar broadening processes recorded when the input polarization is aligned along either of the two principal axes confirms that the fiber core has a low ellipticity and a small birefringence.

These polarization measurements allow us to clearly trace the dynamics of self-shifting Raman solitons and their corresponding blue-shifted dispersive waves [6]. We confirm that soliton generation occurs independently in each fiber axis [26] since no soliton dynamics are observed at the cross-polarization angles corresponding to  $\theta = 90^\circ$  in the  $V$  spectra (figures 3(a) and (d)) and  $\theta = 0^\circ$  in the  $H$  spectra (figures 3(b) and (e)). The cross-polarization geometry also reveals a faint copy of the total output SC. For example, the component at  $\lambda = 800$  nm and  $\theta = 90^\circ$  in figure 3(d) is less intense, by 15 dB, than the corresponding one in figure 3(e). In the same two figures, the components at  $\lambda = 1225$  nm have a difference of 20 dB. We attribute this ‘ghost’ signal to a depolarization effect due to a small, but non-negligible, mechanical stress applied towards the end part of the PCF as we fix it inside a v-groove. Note that any propagation-induced depolarization mechanisms, such as cross-phase modulation (XPM), would produce a blurred copy of the SC spectrum, since solitons and dispersive waves shift in frequency as they propagate along the fiber. Here, we use glue, instead of magnetic clamps, to hold each fiber end to minimize energy transfer into the orthogonally polarized mode. During tests conducted with magnetic clamps instead of glue, ‘ghost’ signals were a factor of 3 larger.

Another interesting feature in the spectra of figure 3 can be observed at  $\theta = -45^\circ$  and  $45^\circ$  (white boxes), where a beating in the spectrum indicates interference and potential crosstalk between the spectral components guided along both principal axes of the fiber. Figures 3(c) and (f) show the DOP calculated from  $\text{DOP} = |P_V - P_H| / (P_V + P_H)$ , where  $P_V$  and  $P_H$  are the total powers, integrated across the full measured spectrum, along the  $V$  and  $H$  directions, respectively. Note that the DOP is not a measure of the optical ellipticity since it does not allow the phase shift between the orthogonal polarization states to be extracted. Since the maximum DOP approaches unity, we can conclude that the fiber can reliably maintain a linear polarization, even in a regime of SC generation extending from 800 to 1200 nm, without a special design inducing stress on the core. More precisely, the maximum value of the DOP is 0.9 at  $\theta = 0^\circ$  and  $90^\circ$ , corresponding to the principal axes. Based on the measured ‘ghost’ signal intensities in figure 3, we can consider a localized decrease in DOP of 0.04 induced by the clamping mechanism at the output end of the fiber. Therefore, depolarization mechanisms due to in-coupling, inhomogeneities, and impurities during optical propagation along the fiber are responsible for a decrease in DOP of 0.06, corresponding to a transfer of 3% of the total energy from one polarization axis to the other.



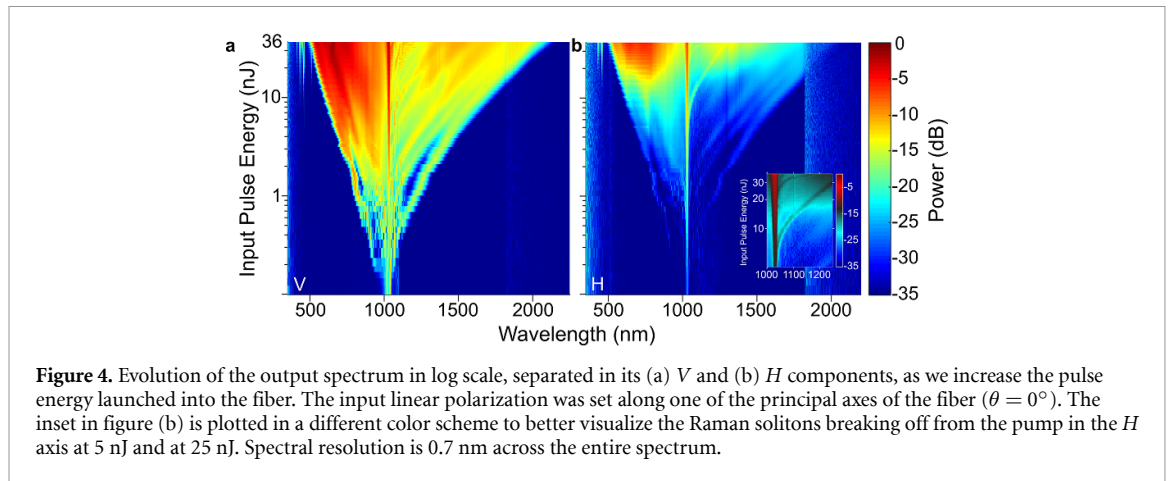


**Figure 4.** Evolution of the output spectrum in log scale, separated in its (a)  $V$  and (b)  $H$  components, as we increase the pulse energy launched into the fiber. The input linear polarization was set along one of the principal axes of the fiber ( $\theta = 0^\circ$ ). The inset in figure (b) is plotted in a different color scheme to better visualize the Raman solitons breaking off from the pump in the  $H$  axis at 5 nJ and at 25 nJ. Spectral resolution is 0.7 nm across the entire spectrum.

In another experiment, we investigate the input pulse energy dependence of the SC while monitoring both orthogonal output polarization components. Here we fix the input polarization to  $\theta = 0^\circ$ , corresponding to the highest DOP measured in figure 3. Results are shown in figure 4 as we increase the input pulse energy from 0.1 to 36 nJ. The unperturbed linear polarization is detected in the  $V$  direction (figure 4(a)), while cross-polarized components are detected in the  $H$  direction (figure 4(b)). We expect analogous results with an input polarization of  $\theta = 90^\circ$ , considering the similar broadening mechanisms and DOP observed for orthogonal input polarizations shown in figure 3.

As we increase the pulse energy, we observe in the  $V$  direction self-shifted Raman solitons breaking off from the pump toward lower frequencies and their corresponding dispersive waves shifting toward higher frequencies [32]. Simultaneously, four-wave mixing broadens the spectral features, flattening out the overall spectrum [26, 32, 33]. As observed in figure 3, the output spectrum in  $V$  produces a ‘ghost’ image in  $H$  because of the small depolarization induced by a mechanical stress from the glue holding the output end of the fiber inside the v-groove. For pulse energies below 5 nJ, spectra measured along  $H$  mainly feature such ‘ghost’ images in addition to a peak at the input pump wavelength. However, above this pump energy, the spectrum shows SPM-like broadening and Raman solitons (inset figure 4(b)) indicating that enough pump energy from  $V$  is scattered into  $H$  to induce strong nonlinear effects.

Using the pulse energy-dependent spectrum measurements in  $V$  and  $H$ , we calculate the total optical power  $P_V$  and  $P_H$  in four spectral windows from which we calculate the DOP. Figure 5(a) shows the DOP obtained by integrating the power over the full spectrum, labeled SC; two 10 nm wide bands at 800 nm and 1500 nm, labeled  $\lambda$  short and  $\lambda$  long, respectively; and an 8 nm wide window centered at  $\lambda = 1030$  nm corresponding to the pump. The spectral width of these three selected windows is comparable to the input pulse bandwidth and they contain enough data points to average out the experimental noise. At pulse energies below  $\sim 10$  nJ, the SC line displays a DOP = 0.9, which agrees well with results shown in figures 3(c) and (f). However, at higher pulse energies, the SC line gradually decreases to 0.4. Previous work has attributed this depolarization to nonlinear interactions [24, 34]. Here we establish a more direct correlation between this reduced DOP and a depolarization mechanism acting preferentially on shorter wavelengths, corresponding to the region that contains the larger portion of the optical power. A comparison between the short and long wavelength ranges allows us to expose this wavelength-dependent depolarization mechanism. For instance, the DOP measured in the  $\lambda$  short region is consistently smaller than the one in the  $\lambda$  long region after an input pulse energy of 7 nJ. More importantly, the  $\lambda$  short line already begins to decrease sharply at 5 nJ while the  $\lambda$  long line remains constant, around 0.9, until 15 nJ. Therefore, we can conclude that short wavelengths are more susceptible to depolarization. Interestingly, the pump line remains stable at DOP  $\sim 0.5$ . We attribute the relatively low DOP at the pump wavelength to the nonlinear redistribution of the spectral weight away from the input wavelength in the  $V$  polarization from SPM, which occurs even at the lowest pulse energies investigated here, while the scattered signal in the  $H$  polarization remains mostly concentrated near the input pump wavelength from depolarization at the input facet of the fiber [35]. These results highlight the importance of evaluating the DOP over the entire spectrum. Simply characterizing the polarization state at the pump wavelength can lead to false conclusions about the polarization properties of an SC source; especially when considering spectra spanning more than an octave.

Figure 5(b) shows the DOP calculated for each spectral component. Here, instead of integrating the spectra to extract  $P_V$  and  $P_H$  and calculate the DOP, the spectra in figure 4, labeled  $S_V(\lambda)$  and  $S_H(\lambda)$  for the spectra in figures 4(a) and (b), respectively, are used directly to calculate the DOP spectrum for all pulse

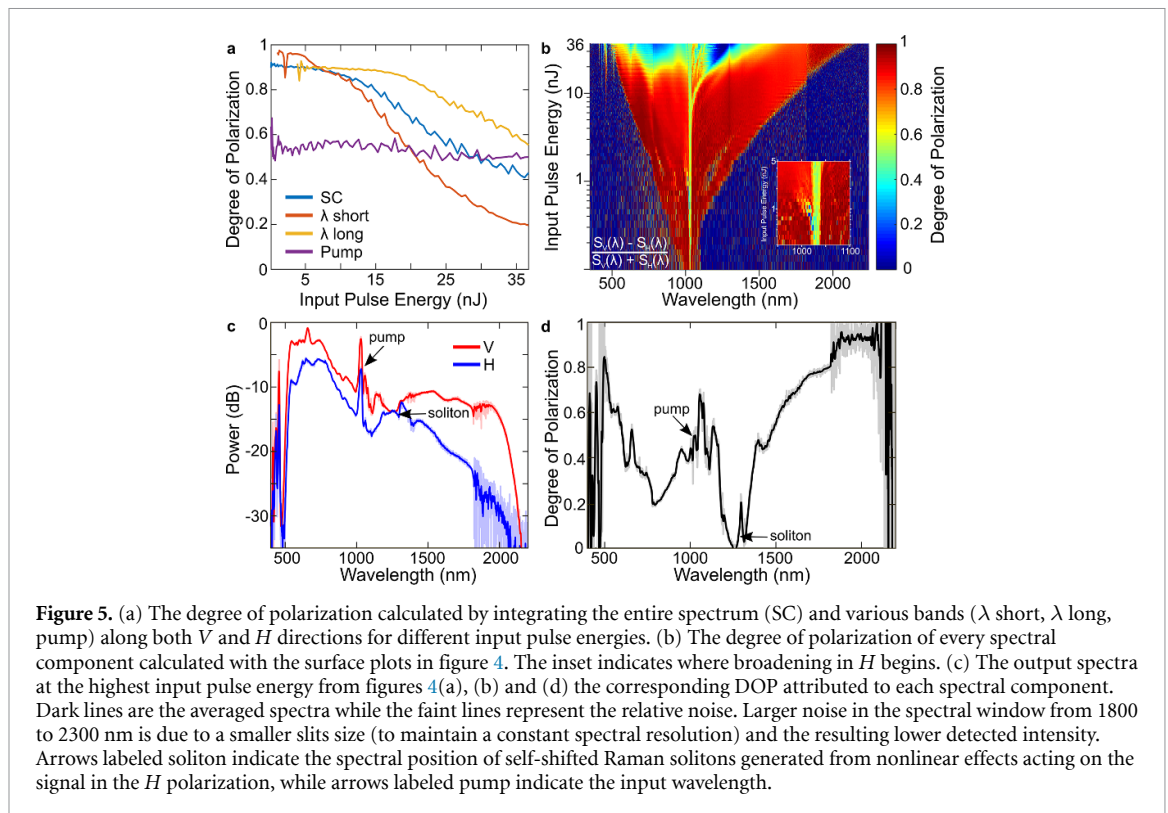


**Figure 5.** (a) The degree of polarization calculated by integrating the entire spectrum (SC) and various bands ( $\lambda$  short,  $\lambda$  long, pump) along both  $V$  and  $H$  directions for different input pulse energies. (b) The degree of polarization of every spectral component calculated with the surface plots in figure 4. The inset indicates where broadening in  $H$  begins. (c) The output spectra at the highest input pulse energy from figures 4(a), (b) and (d) the corresponding DOP attributed to each spectral component. Dark lines are the averaged spectra while the faint lines represent the relative noise. Larger noise in the spectral window from 1800 to 2300 nm is due to a smaller slits size (to maintain a constant spectral resolution) and the resulting lower detected intensity. Arrows labeled soliton indicate the spectral position of self-shifted Raman solitons generated from nonlinear effects acting on the signal in the  $H$  polarization, while arrows labeled pump indicate the input wavelength.

energies. The surface plot reveals not only the overall depolarization trends, but also fine depolarization-related features. For example, at input pulse energies exceeding 5 nJ, we can distinguish a red-shifting spectral region of low DOP corresponding to a Raman soliton in the  $H$  polarization. At 1 nJ, we also trace the depolarization of a gradually blue-shifting component from the pump wavelength (see inset in figure 5(b)). We observe, for all input pulse energies, that the spectral edges of the SC consistently correspond to a localized DOP approaching unity [23, 27]. This result is to be expected because of the nature of nonlinear spectral broadening in optical fibers: shortest and longest wavelengths are generated towards the end facet of the fiber and are thus less susceptible to depolarization effects during optical propagation. The large DOP at the edges of the spectrum is reproduced by numerical simulations (figure S2, supplementary material (available online at [stacks.iop.org/JPPHOTON/3/025002/mmedia](https://stacks.iop.org/JPPHOTON/3/025002/mmedia))) that solve the coupled nonlinear Schrödinger equations, calculate the output spectrum as a function of propagation length in the PCF, and extract the DOP at each wavelength while considering linear and nonlinear depolarization mechanisms. Figure 5(b) also shows, at high pulse energies, a significant decrease of the DOP between 800 and 1400 nm. We can attribute this low DOP to the spectral broadening of the  $H$  polarized component, which notably features self-shifting Raman soliton dynamics above 5 nJ.

Figure 5(c) shows the output spectrum in the  $V$  and  $H$  polarization at the highest pump energy used in the experiment (36 nJ). In the  $V$  direction, the SC extends from 450 to 2150 nm at a 30 dB cutoff. The SC measured in the  $H$  polarization is slightly narrower and shows a pronounced spectral asymmetry caused by a preferential depolarization of the short wavelength components. The arrow labeled soliton indicates the spectral position of self-shifted Raman solitons in the  $H$  polarized signal (see inset of figure 4(b)). The same arrow in figure 5(d) shows a correspondingly low DOP at the same position. The solitons propagate with the same polarization state as the light that generated them [36]. Since the PCF has a relatively low birefringence, the intensity-dependent refractive index associated to a soliton may increase the effective linear birefringence, and therefore reduce depolarization occurring via scattering events. This phenomenon was previously described in a context of a beam injected along the slow axis of a birefringent fiber [37]. This effect could explain the low level of depolarization observed during solitonic propagation and the resulting complex polarization landscape (figure 5(d)) at high power when both orthogonal components independently generated Raman solitons. Figure 5(d) also allows us to clearly observe larger DOP values at longer wavelengths, in comparison to the values at shorter wavelengths, which remain below 0.6.

Lower DOP values at shorter wavelengths shown in figures 5(a) and (d), are consistent with a wavelength-dependent depolarization mechanism, which can be attributed to a Rayleigh scattering effect preferentially acting on shorter wavelengths propagating in the fiber. Such mechanism was previously

proposed to account for the depolarization in fiber communication systems [38]. In our experiment, this effect becomes especially important at high input pulse energies where a large fraction of the optical energy in  $V$  is shifted to the visible region. Numerical simulations (figure S3, supplementary material) establish that linear (scattering effects) and nonlinear (XPM) depolarization mechanisms do not fully explain the wavelength-dependent depolarization we observe experimentally in this work. Note that our results do not directly correlate with the signature  $\lambda^{-4}$ -dependence of Rayleigh scattering caused by emitters smaller than the wavelength. We believe it can be in part attributed to depolarization effects caused by defects of different sizes in the fiber and also to the spatial mode distribution at shorter wavelengths, which is better confined in the center of the core and therefore less sensitive to structural deformations occurring at the air-core interface.

## 4. Conclusion

In this work, we introduce a novel technique to measure the SC generated in each fiber axis of a highly nonlinear fiber and investigate wavelength-dependent polarization properties. We collect output spectra for varying input polarization states and pulse energies, allowing us to confirm that Raman soliton and dispersive wave generation remain axis-specific as they propagate along our low-birefringent PCF. Measurements also reveal that the edges of the SC have a consistently larger DOP than the central region near the pump. More specifically, we identify a depolarization mechanism indicative of Rayleigh-like scattering preferentially reducing the DOP at shorter wavelengths. In summary, our results and analysis show the importance of characterizing the polarization properties of every spectral component when using fiber-based broadband radiation. Such information is not attainable using conventional measurement techniques based on standard OSAs. We believe that our versatile experimental configuration is the most accurate method to date for quantifying the polarization maintaining ability of optical fibers, as it provides an in-depth understanding of the relationship between spectral broadening and depolarization effects over all frequencies of an SC. In the future, elliptical-sensitive detection could be readily implemented in such a setup to allow for the full polarization characterization of each spectral component. This system could then retrieve a relevant set of parameters to describe twisted fibers, which are optimized to guide circularly polarized light and exhibit exotic polarization properties [39, 40].

## Acknowledgments


The authors are grateful for the technical assistance provided by Shyamal Das, Anirban Dhar and Mrinmay Pal to fabricate the photonic crystal fiber. We also acknowledge the NSERC-Canada Graduate Scholarship, Ontario Graduate Scholarship, NSERC Discovery program and the Canada Foundation for Innovation (Project Number 35269). Professor A K Kar would like to acknowledge the support of UK Engineering and Physical Sciences Research Council (Project CHAMP, EP/M015130/1). Dr M C Paul acknowledges the support of CSIR-CGCRI and the DST-Inspired Research (INSPIRE) Fellowship (IF150744) as well as the Newton-Bhabha Fellowship of P H Reddy awarded by the British Council, UK.

## ORCID iDs

Nicolas Couture  <https://orcid.org/0000-0002-7137-8102>

Rachel Ostic  <https://orcid.org/0000-0002-1634-0478>

P Harshavardhan Reddy  <https://orcid.org/0000-0002-8799-6060>

Mukul Chandra Paul  <https://orcid.org/0000-0001-8805-6129>

Jean-Michel Ménard  <https://orcid.org/0000-0002-6458-758X>

## References

- [1] Jiao K *et al* 2019 Mid-infrared flattened supercontinuum generation in all-normal dispersion tellurium chalcogenide fiber *Opt. Express* **27** 2036–43
- [2] Jiang Z, Wang T, Sun Z, Chen J, Zhang X, Lin P, Chen P and Zhao Y 2019 Partially coherent seeding of supercontinuum generation in picosecond regime *Opt. Laser Technol.* **120** 105752
- [3] Poudel C and Kaminski C F 2019 Supercontinuum radiation in fluorescence microscopy and biomedical imaging applications *J. Opt. Soc. Am. B* **36** A139–A153
- [4] Borondics F, Jossent M, Sandt C, Lavoute L, Gaponov D, Hideur A, Dumas P and Février S 2018 Supercontinuum-based Fourier transform infrared spectromicroscopy *Optica* **5** 378–81
- [5] Dupont S, Petersen C, Thøgersen J, Agger C, Bang O and Keiding S R 2012 IR microscopy utilizing intense supercontinuum light source *Opt. Express* **20** 4887–92



- [6] Travers J C, Chang W, Nold J, Joly N Y and Russell P S J 2011 Ultrafast nonlinear optics in gas-filled hollow-core photonic crystal fibers [Invited] *J. Opt. Soc. Am. B* **28** A11–A26
- [7] Köttig F, Novoa D, Tani F, Günendi M C, Cassataro M, Travers J C and Russell P S J 2017 Mid-infrared dispersive wave generation in gas-filled photonic crystal fibre by transient ionization-driven changes in dispersion *Nat. Commun.* **8** 813
- [8] Cassataro M, Novoa D, Günendi M C, Edavalath N N, Frosz M H, Travers J C and Russell P S J 2017 Generation of broadband mid-IR and UV light in gas-filled single-ring hollow-core PCF *Opt. Express* **25** 7637–44
- [9] Belli F, Abdolvand A, Chang W, Travers J C and Russell P S J 2015 Vacuum-ultraviolet to infrared supercontinuum in hydrogen-filled photonic crystal fiber *Optica* **2** 292–300
- [10] Qin G, Yan X, Kito C, Liao M, Chaudhari C, Suzuki T and Ohishi Y 2009 Ultrabroadband supercontinuum generation from ultraviolet to 6.28  $\mu\text{m}$  in a fluoride fiber *Appl. Phys. Lett.* **95** 161103
- [11] Swiderski J, Michalska M and Mazé G 2013 Mid-IR supercontinuum generation in a ZBLAN fiber pumped by a gain-switched mode-locked Tm-doped fiber laser and amplifier system *Opt. Express* **21** 7851–7
- [12] Xia C, Kumar M, Kulkarni O P, Islam M, Terry J F L, Freeman M J, Poulain M and Mazé G 2006 Mid-infrared supercontinuum generation to 4.5  $\mu\text{m}$  in ZBLAN fluoride fibers by nanosecond diode pumping *Opt. Lett.* **31** 2553–5
- [13] Jiang X, Joly N Y, Finger M A, Babic F, Wong G K L, Travers J C and Russell P S J 2015 Deep-ultraviolet to mid-infrared supercontinuum generated in solid-core ZBLAN photonic crystal fibre *Nat. Photon.* **9** 133–9
- [14] Saghaei H, Moravvej-Farshi M K, Ebnali-Heidari M and Moghadasi M N 2016 Ultra-wide mid-infrared supercontinuum generation in  $\text{As}_{40}\text{Se}_{60}$  chalcogenide fibers: solid core PCF versus SIF *IEEE J. Sel. Top. Quantum Electron.* **22** 279–86
- [15] Wei D P, Galstian T V, Smolnikov I V, Plotnichenko V G and Zohrabyan A 2005 Spectral broadening of femtosecond pulses in a single-mode As–S glass fiber *Opt. Express* **13** 2439–43
- [16] Kubat I et al 2014 Mid-infrared supercontinuum generation to 12.5  $\mu\text{m}$  in large NA chalcogenide step-index fibres pumped at 4.5  $\mu\text{m}$  *Opt. Express* **22** 19169–82
- [17] Hudson D D, Antipov S, Li L, Alamgir I, Hu T, Amraoui M E, Messaddeq Y, Rochette M, Jackson S D and Fuerbach A 2017 Toward all-fiber supercontinuum spanning the mid-infrared *Optica* **4** 1163–6
- [18] Yang L, Zhang B, Yin K, Yao J, Liu G and Hou J 2016 0.6–3.2  $\mu\text{m}$  supercontinuum generation in a step-index germania-core fiber using a 4.4 kW peak-power pump laser *Opt. Express* **24** 12600–6
- [19] Jain D, Sidharthan R, Moselund P M, Yoo S, Ho D and Bang O 2016 Record power, ultra-broadband supercontinuum source based on highly  $\text{GeO}_2$  doped silica fiber *Opt. Express* **24** 26667–77
- [20] Monerie M and Jeunhomme L 1980 Polarization mode coupling in long single-mode fibre *Opt. Quantum Electron.* **12** 449–61
- [21] de Boer J F, Hitznerberger C K and Yasuno Y 2017 Polarization sensitive optical coherence tomography—a review [Invited] *Biomed. Opt. Express* **8** 1838–73
- [22] Herrera R A 2017 Influence of the wavelength dependence of birefringence in the generation of supercontinuum and dispersive wave in fiber optics *Math. Probl. Eng.* **2017** 3517407
- [23] Zhu Z and Brown T G 2004 Experimental studies of polarization properties of supercontinua generated in a birefringent photonic crystal fiber *Opt. Express* **12** 791–6
- [24] Tu H, Liu Y, Liu X, Turchinovich D, Lægsgaard J and Boppart S A 2012 Nonlinear polarization dynamics in a weakly birefringent all-normal dispersion photonic crystal fiber: toward a practical coherent fiber supercontinuum laser *Opt. Express* **20** 1113–28
- [25] Chao Q and Wagner K H 2015 Polarization instability of Raman solitons ejected during supercontinuum generation *Opt. Express* **23** 33691–704
- [26] Proulx A, Ménard J-M, Hô N, Laniel J M, Vallée R and Paré C 2003 Intensity and polarization dependences of the supercontinuum generation in birefringent and highly nonlinear microstructured fibers *Opt. Express* **11** 3338–45
- [27] Tarnowski K, Martynkien T, Mergo P, Poturaj K, Anuszkiewicz A, Bójot P, Billard F, Faucher O, Kibler B and Urbanczyk W 2017 Polarized all-normal dispersion supercontinuum reaching 2.5  $\mu\text{m}$  generated in a birefringent microstructured silica fiber *Opt. Express* **25** 27452–63
- [28] Sopalla R P, Wong G K L, Joly N Y, Frosz M H, Jiang X, Ahmed G and Russell P S J 2019 Generation of broadband circularly polarized supercontinuum light in twisted photonic crystal fibers *Opt. Lett.* **44** 3964–7
- [29] Jiang X, Euser T G, Abdolvand A, Babic F, Tani F, Joly N Y, Travers J C and Russell P S J 2011 Single-mode hollow-core photonic crystal fiber made from soft glass *Opt. Express* **19** 15438–44
- [30] Reddy P H, Kir'yanov A V, Dhar A, Das S, Dutta S, Pal M, Barmenkov Y M, Minguella-Gallardo J A, Bhadra S K and Paul M C 2017 Fabrication of ultra-high numerical aperture  $\text{GeO}_2$ -doped fiber and its use for broadband supercontinuum generation *Appl. Opt.* **56** 9315–24
- [31] Noda J, Okamoto K and Sasaki Y 1986 Polarization-maintaining fibers and their applications *J. Lightwave Technol.* **4** 1071–89
- [32] Dudley J M, Genty G and Coen S 2006 Supercontinuum generation in photonic crystal fiber *Rev. Mod. Phys.* **78** 1135
- [33] Dudley J M and Taylor R 2010 *Supercontinuum Generation in Optical Fibers* (Cambridge: Cambridge University Press) (<https://doi.org/10.1017/CBO9780511750465>)
- [34] Domingue S R and Bartels R A 2013 Overcoming temporal polarization instabilities from the latent birefringence in all-normal dispersion, wave-breaking-extended nonlinear fiber supercontinuum generation *Opt. Express* **21** 13305–21
- [35] Chick B J, Chon J W M and Gu M 2008 Polarization effects in a highly birefringent nonlinear photonic crystal fiber with two-zero dispersion wavelengths *Opt. Express* **16** 20099–105
- [36] Flores-Rosas A, Peralta-Hernandez J I, Bracamontes-Rodríguez J E, Villagomez-Bernabe B A, Beltrán-Pérez G, Pottiez O, Ibarra-Escamilla B, Rojas-Laguna R and Kuzin E A 2014 Observation of a high grade of polarization of solitons generated in the process of pulse breakup in a twisted fiber *J. Opt. Soc. Am. B* **31** 821–6
- [37] Winful H G 1986 Polarization instabilities in birefringent nonlinear media: application to fiber-optic devices *Opt. Lett.* **11** 33–35
- [38] Barfuss H and Brinkmeyer E 1986 Polarization holding and anisotropic Rayleigh scattering in birefringent single-mode fibers *J. Opt. Soc. Am. A* **3** 426–31
- [39] Palmieri L 2006 Polarization properties of spun single-mode fibers *J. Lightwave Technol.* **24** 4075–88
- [40] Wong G K L, Kang M S, Lee H W, Biancalana F, Conti C, Weiss T and Russell P S J 2012 Excitation of orbital angular momentum resonances in helically twisted photonic crystal fiber *Science* **337** 446–9